Research Article

ADVANCED PHOTONICS

Arbitrary control of the flow of light using pseudomagnetic fields in photonic crystals at telecommunication wavelengths

Pan Hu,[a] Lu Sun,[a,*] Ce Chen,[a] Jingchi Li,[a] Xiong Ni,[a] Xintao He,[b] Jianwen Dong,[b,*] and Yikai Su[a,*]
[a]Shanghai Jiao Tong University, Department of Electronic Engineering, State Key Laboratory of Photonics and Communications, Shanghai, China
[b]Sun Yat-sen University, State Key Laboratory of Optoelectronic Materials and Technologies, School of Physics, Guangzhou, China

Abstract. Pseudomagnetic fields (PMFs) can manipulate photons in a similar way that magnetic fields control electrons. However, the PMF-based control over light has been restricted to simple waveguiding of the Landau level states, which hinders the application of PMFs in practical photonic integrated circuits. Here, we propose a universal and systematic methodology to design complex nonuniform PMFs and arbitrarily control the flow of light in silicon photonic crystals at telecommunication wavelengths. As proofs of concept, an S-bend (with a low insertion loss of <1.83 dB) and a 50:50 power splitter (with a low excess loss of <2.11 dB and imbalance of less than ±0.5 dB) based on PMFs are experimentally demonstrated. A high-speed data transmission experiment is performed on these devices with 140-Gb/s four-level pulse amplitude modulation signals to prove their applicability in real communication systems. The proposed method offers a paradigm for exploring magnetic-field-related physics with neutral particles and developing nanophotonic devices with PMF-induced states beyond the Landau level states and the topological edge states.

Keywords: pseudomagnetic fields; Landau level states; topological photonics.

Received Mar. 10, 2025; revised manuscript received Jul. 14, 2025; accepted for publication Aug. 7, 2025; published online Sep. 1, 2025.

[DOI: 10.1117/1.AP.7.6.066001]

1 Introduction

In condensed-matter physics, many intriguing phenomena can be observed for electrons under external magnetic fields, e.g., the quantum Hall effect and the Landau levels.[1–12] These phenomena play a pivotal role in shaping our understanding of the topological phases of matter.[13–16] However, neutral particles, such as photons and cold atoms, barely interact with magnetic fields. Although the magneto-optic effects are strong enough at microwave frequencies to effectively mediate the interactions between photons and magnetic fields,[17,18] the magneto-optic coefficients of natural materials are too weak at optical frequencies, making the magnetic-field-associated effects inaccessible in on-chip nanophotonic systems. Pseudomagnetic fields (PMFs), also known as artificial gauge fields, have been proposed to mimic the behaviors of electrons under magnetic fields in classical wave systems.[19–40] Recently, Landau levels and Landau rainbow were realized in two-dimensional (2D) photonic crystals (PhCs) by inducing PMFs via synthetic strain or breaking local spatial inversion symmetry in each unit cell.[41–44] Spin- and valley-Hall effects were also observed in photonic Dirac waveguides and cavities.[45–48] However, these works focus on the Landau levels and the behaviors of the related chiral states similar to those of the topological edge states in topological PhCs. A systematic method based on PMFs for more flexible control over light is still missing, which hinders their application in practical photonic integrated circuits where more complicated functions (such as arbitrary splitting and routing of light) are necessary.

Here, we go beyond the Landau levels and the chiral states and propose a universal design method for PMFs that can realize arbitrary control of the flow of light in silicon PhCs at telecommunication wavelengths. By changing the local spatial-inversion-symmetry-breaking strength at every point in PhCs, effective PMFs with arbitrary distributions can be designed at

*Address all correspondence to Lu Sun, sunlu@sjtu.edu.cn; Jianwen Dong, dongjwen@mail.sysu.edu.cn; Yikai Su, yikaisu@sjtu.edu.cn

will and introduced into dielectric photonic systems without breaking the real-time reversal symmetry. The supported modes and the propagation of light in the PhCs with the synthetic PMFs are theoretically and experimentally investigated. As examples of routing and splitting light using PMFs, an S-bend with a low insertion loss (IL) of <1.83 dB and a 50:50 power splitter with a low excess loss (EL) of <2.11 dB and imbalance of less than ±0.5 dB are proposed and experimentally demonstrated. To prove the applicability of these functional devices based on PMFs in practical on-chip photonic systems, we conduct a high-speed data transmission experiment with a 140-Gb/s four-level pulse amplitude modulation (PAM-4) signal per channel. To the best of our knowledge, this is the first time that a systematic method is proposed to synthesize PMFs for arbitrarily controlling the flow of light and realizing various functional devices for on-chip optical communications. Our work provides a novel design paradigm to address the pivotal challenge of low-loss and high-density interconnects in photonic integrated circuits. More importantly, it offers a versatile platform for exploring fundamental physics such as emulating quantum phenomena under complex gauge fields. These findings pave the way toward developing a new class of nanophotonic devices with PMFs, which may find applications in many fields including optical communications, optical computing, quantum information processing, and beyond.

2 Results

2.1 Realization of Pseudomagnetic Fields in Photonic Crystals

Figure 1(a) shows a schematic of the PhC with a honeycomb lattice implemented on the silicon-on-insulator (SOI) platform. The unit cell is illustrated in the red-dashed rhombic boxes and contains two inverted equilateral triangular holes with side lengths d_1 and d_2. The lattice constant is a_0. When the spatial inversion symmetry is unbroken ($d_1 = d_2$), the PhC lattice exhibits a C_{6v} symmetry, featuring a Dirac cone at the K and K' points in the momentum space, as shown by the band diagram of the transverse electric (TE) modes of the PhC in the middle of Fig. 1(a). Using the plane wave expansion method and applying the $\vec{k}\cdot\vec{p}$ approximation,[49–56] the two lowest bands can be described analytically by an effective Hamiltonian near the K/K' points: $H_{K/K'} = \pm(vk_x\sigma_x + vk_y\sigma_y)$, where $\pm$ represents the K (K') valley pseudospin, $\sigma_{x,y,z}$ denotes the Pauli matrices, v is the group velocity, and (k_x, k_y) is the reciprocal vector with respect to the degeneracy points K and K' (see Sec. 1 in the Supplementary Material for more details). By introducing asymmetry between the sizes of the two holes within the unit cell ($d_1 \neq d_2$), the spatial inversion symmetry is broken, and the lattice symmetry is reduced from C_{6v} to C_{3v}. An effective mass term m is introduced to the Dirac cone, which lifts the Dirac degeneracy and opens a bandgap of $\Delta\omega = 2|m|$, as shown on the right of Fig. 1(a). More details about the effective mass and the size difference of the triangular holes can be found in Sec. 2 in the Supplementary Material. If the mass term varies with position, the effective Hamiltonian becomes

$$H_{K/K'} = \pm[vk_x\sigma_x + vk_y\sigma_y + m(\vec{r})\sigma_z], \quad (1)$$

where $m(\vec{r})$ is the position-dependent mass term. Considering a Hamiltonian describing the interaction between the Dirac quasiparticles and the synthetic gauge field A_z, it should take the form $H_{K/K'} = \pm(vk_x\sigma_x + vk_y\sigma_y + p_z\sigma_z)$, where $p_z = k_z + A_z$ corresponds to the canonical momentum in the presence of the magnetic field. By comparing it with Eq. (1) and noticing that $k_z = 0$ in the case of 2D PhCs discussed here, the effective mass term is equivalent to a magnetic vector potential, i.e., $A_z = m(\vec{r})$. For a linearly varying mass term $m(x) = ax$, it corresponds to a PMF $B_y = -a$, which gives rise to the celebrated Landau levels. Most importantly, the fields of the chiral states of the Landau levels will be confined to the vicinity of the area that satisfies $p_z = 0$ or equivalently $A_z = 0$. The gauge invariance allows us to choose different magnetic vector potentials for the same PMF.[57] However, as we can see, the other forms of magnetic vector potentials are difficult to realize in 2D PhCs (see Sec. 3 in the Supplementary Material for details). Different from topological edge states, the Landau level states are propagative bulk states, which are also topologically protected. Figure 1(b) shows the PhC structure, band diagram, and Bloch mode profile of the zeroth-order Landau level in one period along the y direction. In the x direction, the side length of the triangular holes d_1 (d_2) increases (decreases) linearly, as shown in the supercell encircled by the red-dashed boxes. The red and green dotted lines in the band diagram represent the chiral states of the zeroth-order Landau level at the K and K' points, respectively. The propagation directions of the chiral states are dependent on the phase vortices of the excitation sources (see Sec. 4 in the Supplementary Material for details). As the zeroth-order Landau levels are well separated from the higher-order ones (black dotted lines) in frequency, the corresponding states are easy to excite and remain single-mode during propagation. Hereafter, we choose to work with the zeroth-order Landau level to construct various nanophotonic devices in silicon PhCs. The states of the zeroth-order Landau level are approximately linearly dispersive, and the dispersion relationship can be expressed as $\omega_{K/K'} = \pm\mathrm{sgn}(B_y)vk_y$,[30,44] where $\omega_{K/K'}$ is the frequency of the mode in the K (K') valley, and $\mathrm{sgn}(B_y)$ is the sign of the synthetic magnetic field. The bottom of Fig. 1(b) shows the H_z field distribution of the state corresponding to the blue star point on the green dotted line in the band diagram. Obviously, the field is highly localized near $x = 0$ [purple shaded area in Fig. 1(b)] where the condition $A_z = 0$ is satisfied. The expression of the state can be derived by solving Eq. (1) (see Sec. 1 in the Supplementary Material for details),

$$\psi(x,y) = \frac{1}{\sqrt{2}}\begin{pmatrix}1\\ i\end{pmatrix}e^{ik_y y}e^{-\frac{1}{v}\int m(x)\mathrm{d}x} = \frac{1}{\sqrt{2}}\begin{pmatrix}1\\ i\end{pmatrix}e^{\frac{-a}{2v}x^2}e^{ik_y y}. \quad (2)$$

The state shows the behavior of a propagating wave along the y direction and the characteristics of a Gaussian wave along the x direction, indicating the existence of a propagative bulk state near $x = 0$. Moreover, the field distribution of the state is directly related to the effective mass term, i.e., $\psi(x,y) \propto e^{-\frac{1}{v}\int m(x)\mathrm{d}x}$, which means the confinement of light near $x = 0$ is guaranteed as long as $m(x)$ is an odd function such as $m(x) = ax^{1/3}$ and $m(x) = ax^3$, and can be tuned by choosing different functions for $m(x)$ (see Sec. 5 in the Supplementary Material for details). In Fig. 1(c), we show another example with a linearly varying mass term $m(y) = by$, which corresponds to a PMF $B_x = b$. The side length of the triangular holes d_1 (d_2) decreases (increases) linearly in the y direction, as shown in the supercell in the red-dashed boxes.

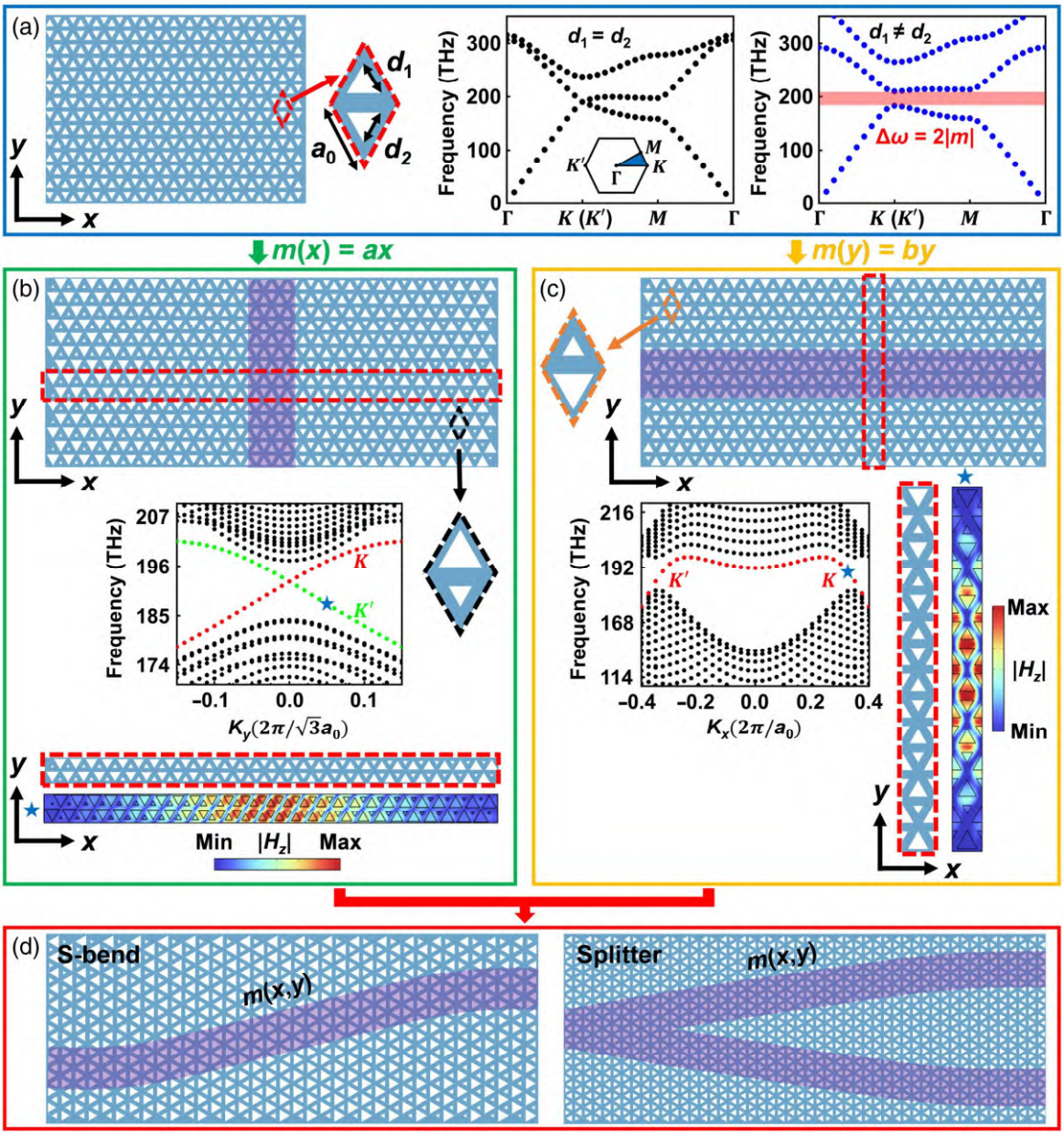

Fig. 1 Realization of PMFs in PhCs. (a) Schematic of the pristine PhC with a honeycomb lattice (left) and band diagrams of the PhCs with C_{6v} symmetry (middle) and C_{3v} symmetry (right). The rhombic unit cell is encircled by the red-dashed line. The first Brillouin zone is shown in the inset of the band diagram. (b) and (c) Schematics of the PhCs (top), band diagrams of the supercells encircled by the red-dashed line (middle/bottom left), and mode profiles corresponding to the blue star points in the band diagrams (bottom/bottom right) with inhomogeneous effective mass terms (b) $m(x) = ax$ and (c) $m(y) = by$. The propagation paths of light are shaded in purple. The rhombic unit cells in panels (b) and (c) are encircled by the black and orange dashed lines, respectively. (d) Schematics of the S-bend (left) and the power splitter (right) based on PMFs, with the propagation paths of light shaded in purple.

The red dotted line in the band diagram represents the propagative bulk states of the zeroth-order Landau level. The profile of the mode corresponding to the blue star point is shown on the bottom right of Fig. 1(c). As one can see, the field is well confined to the region near $y = 0$ [purple-shaded area in Fig. 1(c)]. More details about the propagative bulk states under such a PMF can be found in Sec. 1 in the Supplementary Material.

By synthesizing uniform magnetic fields, one can realize the Landau levels and the straight waveguiding of light in the x and y directions. However, more complicated manipulation of light waves is required for constructing photonic integrated circuits

for real applications. We go beyond the Landau levels and design complex nonuniform PMFs to flexibly control the flow of light on a chip, as shown in Fig. 1(d). By introducing a nonuniform PMF varying in both the x and y directions, the deflection of light can be realized and exploited to build an S-bend in a PhC platform, as indicated by the purple-shaded stripe on the left of Fig. 1(d). Different from the sharp bends that exploit the spin- and valley-Hall effects,[45,49] the S-bend is solely determined by the predefined PMF and therefore provides more flexibility in designing the optical path. Furthermore, the field distribution of the propagative bulk state can be engineered by judiciously designing the PMF through the relationship $\psi(x,y) \propto e^{-\frac{1}{v}\int m(x,y)\mathrm{d}x}$. In other words, once the light path or the field distribution function $\psi(x,y)$ is given, one can derive the corresponding effective mass distribution $m(x,y)$ by taking the first-order derivative of $\psi(x,y)$ with respect to the spatial coordinate x. This method can be employed to build a power splitter with a splitting ratio of 50:50 in a PhC platform, as schematically illustrated on the right side of Fig. 1(d). The light paths in the PhC are shaded in purple as a guide to the eye. The design and the implementation of the PMFs for these two devices will be detailed in Sec. 2.2. Most importantly, we argue that the methodology presented here is universal and systematic. A new family of nanophotonic devices can be developed by designing and synthesizing nonuniform PMFs with this method.

2.2 Device Design and Experimental Demonstration

We start with the straightforward-propagating states of the zeroth-order Landau levels under the uniform PMFs $m(x) = ax$ and $m(y) = by$. The design details, simulation results, and experimental results are given in Sec. 6 in the Supplementary Material. The ILs of the two devices are lower than 1.32 and 0.8 dB in the wavelength range of 1520 to 1580 nm, manifesting the capability of on-chip waveguiding for these two kinds of PMFs. Then, we move on to the more general cases where the more sophisticated nonuniform PMFs are designed and implemented for various basic functional devices such as an S-bend and a power splitter. Figure 2(a) shows a schematic of a PhC-based S-bend operating at telecommunication wavelengths, which is built on an SOI platform with a 220-nm-thick top silicon layer, a 3-μm-thick buried oxide layer, and a 1-μm-thick silica upper cladding layer. The PMF is designed to be $m(x,y) = cx + d$ in region I, $m(x,y) = ax + by$ $(b/a = -10)$ in region II, and $m(x,y) = cx - d$ in region III. It leads to a zero magnetic vector potential $A_z = 0$ on the line $x = -d/c$ in region I, $y = -ax/b$ in region II, and $x = d/c$ in region III, which

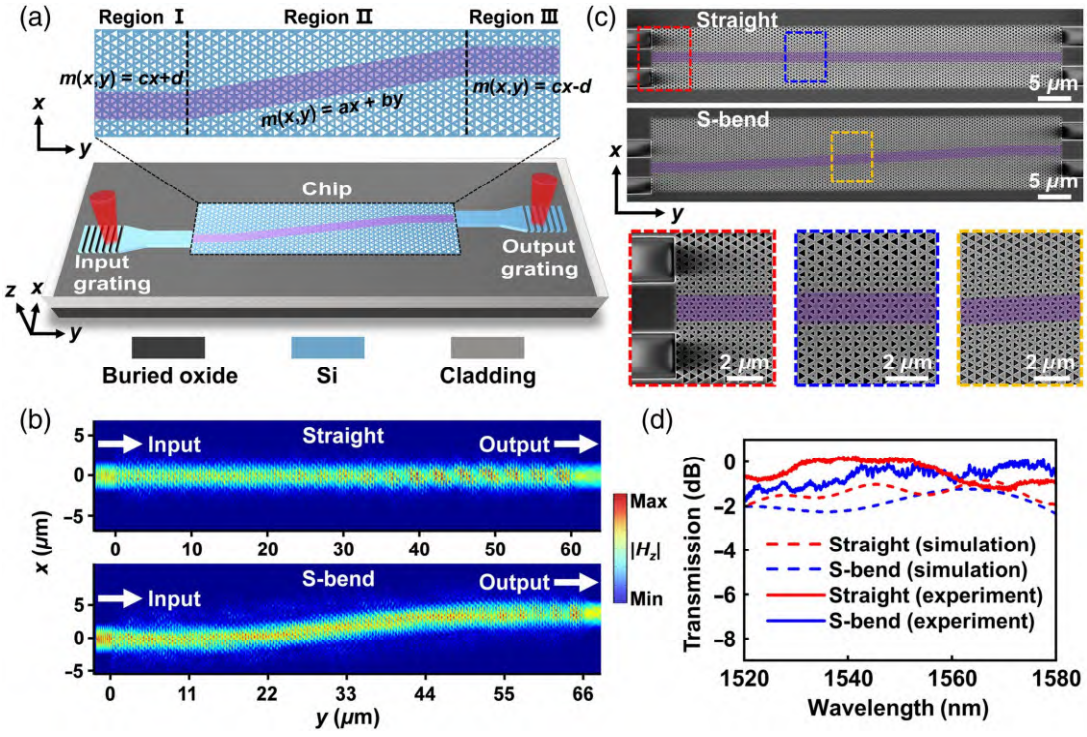

Fig. 2 Demonstration of a straight waveguide and an S-bend based on PMFs. (a) Schematic of the S-bend implemented on an SOI platform. The purple-shaded area indicates the propagation path of light. Light is coupled into and out of the chip by grating couplers. (b) Simulated propagation profiles for the straight waveguide with $m(x) = ax$ (top) and the S-bend with a nonuniform PMF (bottom) at a central wavelength of 1550 nm. (c) SEM images of the fabricated devices. The purple-shaded areas indicate the propagation paths of light. The areas encircled by the red, blue, and orange dashed boxes are zoomed in and displayed at the bottom of the figure. (d) Simulated and measured transmission spectra of the straight waveguide and the S-bend.

defines the propagation path of light in the PhC as indicated by the purple shaded stripe in Fig. 2(a). We choose $b/a = -10$ for region II to achieve a small bending radius and a relatively low IL at the same time. The trade-off between the bending radius (the partition abruptness) and the IL is discussed in Sec. 7 in the Supplementary Material. The lattice constant of the PhC is $a_0 = 450$ nm. The side lengths of the triangular holes d_1 and d_2 are 225 nm on the propagation path line and change linearly with a variation step of 14.7 nm ($\Delta d_1 = -\Delta d_2 = 14.7$ nm) along the direction perpendicular to the line. The light is coupled into and out of the chip by grating couplers, as illustrated in Fig. 2(a). The PhC structure is connected to the grating couplers via two 3 μm-wide silicon stripe waveguides whose fundamental TE mode excites the zeroth-order propagative bulk state in the PhC. To prove that the bending of light based on the nonuniform PMF works as well as the straight waveguiding of the Landau level state under the uniform PMF, we used the three-dimensional finite-difference time-domain (3D FDTD) methods to simulate the propagation of light in both the straight waveguide and the S-bend. Figure 2(b) presents the simulated propagation profiles for the two devices at the wavelength of 1550 nm. It is evident that the light propagates along an S-shaped trajectory predefined by $A_z = 0$ in a nonuniform PMF just as in the case of a straight PhC waveguide, which is in good agreement with our theoretical prediction. These devices were also fabricated on the SOI platform using complementary metal-oxide-semiconductor (CMOS)-compatible process (the fabrication details can be found in Sec. 8 in the Supplementary Material).[58–60] The scanning electron microscopy (SEM) images of the fabricated devices are displayed in Fig. 2(c), with the light propagation paths shaded in purple as a guide to the eye. The zoomed-in images of the interface between the silicon stripe waveguide and the PhC, the area around $x = 0$ of the straight PhC waveguide, and the area in the proximity of the propagation path in region II of the S-bend are shown in the red, blue, and orange dashed boxes on the bottom of Fig. 2(c). By employing a scanning near-field optical microscope (SNOM) system with atomic force microscope tips which offers a high resolution of ~20 nm, the light propagation routes in the PhCs can be directly monitored.[61] However, due to the lack of such an equipment in our lab, we did not perform the SNOM experiment here. Figure 2(d) shows the simulated and measured transmission spectra of both devices. The measured transmission spectra are all normalized to that of a pair of reference grating couplers fabricated on the same chip (see Sec. 9 in the Supplementary Material for the measurement details). The measured ILs of the straight waveguide and the S-bend are lower than 1.32 and 1.83 dB, respectively, in the wavelength range of 1520 to 1580 nm, which are in reasonable agreement with the simulated ILs of <2 dB (straight waveguide) and <2.27 dB (S-bend). Lower ILs can be reached by optimizing the variation step Δd_1 and the width of the silicon stripe waveguide W_{Si} to maximize the mode overlap between the silicon stripe waveguide and the PhC (see Sec. 10 in the Supplementary Material for more details). We argue that the ILs mainly originate from the coupling losses at the interfaces between the silicon stripe waveguide and the PhC structure while the propagation losses inside the PhC are negligible. It is noteworthy that the S-bend structure introduces almost no extra losses as compared with the straight waveguide, confirming the feasibility of achieving low-loss nanophotonic devices with as-designed nonuniform PMFs. To further demonstrate the universality of this PMF design method, we also simulate a straight waveguide and an S-bend based on PhCs with circular holes (see Sec. 11 in the Supplementary Material for more details).

Next, we present another example of a 50:50 power splitter to show how to design the nonuniform PMF according to the light field distribution $\psi(x, y)$. Figure 3(a) shows a schematic of the consecutive supercells of the power splitter along the propagation direction. The field of the propagative bulk state is initially localized around $x = 0$ and gradually becomes concentrated on two well-separated positions in a supercell, as indicated by the red Gaussian-like wave packets in Fig. 3(a). The separation between the two maxima of the field grows linearly with propagation distance, implementing the splitting of light during propagation. The relationship between the light field and the PMF can be described by $\psi(x, y) \propto e^{-\frac{1}{v}\int m(x,y)\mathrm{d}x}$ (see Sec. 1 in the Supplementary Material for details). By taking the first-order derivatives of $\psi(x, y)$ with respect to the spatial coordinate x, one can obtain the effective mass distribution $m(x, y)$ in every supercell, as shown on the bottom of Fig. 3(a). The two zeros of the mass term separate slowly along the propagation direction. The whole structure of the power splitter is schematically illustrated in Fig. 3(b) where the propagation paths of light are shaded in purple. The lattice constant of the PhC is $a_0 = 450$ nm. The side lengths of the triangular holes d_1 and d_2 are 225 nm on the propagation paths where $A_z = 0$ and change gradually with a variation step of 6.9 nm away from the paths to mimic the nonuniform PMF described above (the relationship between the effective mass term and the sizes of the triangular holes can be found in Sec. 2 in the Supplementary Material). Full-wave numerical simulations were carried out using the 3D FDTD methods to investigate the propagation of light in the power splitter. Figure 3(c) shows the propagation profile for the device at the wavelength of 1550 nm. The zeroth-order propagative bulk state is excited by the fundamental TE mode in a silicon stripe waveguide, split equally into two beams in the PhC, and output from two silicon stripe waveguides. Again, the proposed device was fabricated with a CMOS-compatible process. Figure 3(d) presents the SEM images of the fabricated device, with the purple-shaded area indicating the light propagation paths. The zoomed-in images of the input port, splitting area, and output ports are displayed in the red, blue, and orange dashed boxes, respectively, at the bottom of Fig. 3(d). The simulated and measured transmission spectra of the device are plotted in Fig. 3(e). In the simulations, the imbalance of the power splitter is close to 0 dB, and the EL is below 2.06 dB in the wavelength range of 1527 to 1573 nm. In the experiments, the measured imbalance and EL are lower than ± 0.5 and 2.11 dB, respectively, in the same wavelength range, which is in good agreement with the simulation results. Moreover, the EL of the power splitter is comparable to the ILs of the straight waveguide and the S-bend shown in Fig. 2, proving that the EL mainly comes from the coupling loss between the silicon stripe waveguide and the PhC, and the beam splitting process causes rare extra losses. More importantly, the arbitrary control of the flow of light with PMFs can be envisioned as both the light field distribution and the corresponding PMF can be designed at will using our method. For example, we also demonstrate power splitters with arbitrary splitting ratios by adjusting the distribution of the effective mass term $m(x, y)$. The simulation details are provided in Sec. 12 in the Supplementary Material. In addition, to further verify that other functional devices can also be constructed through this mechanism, we

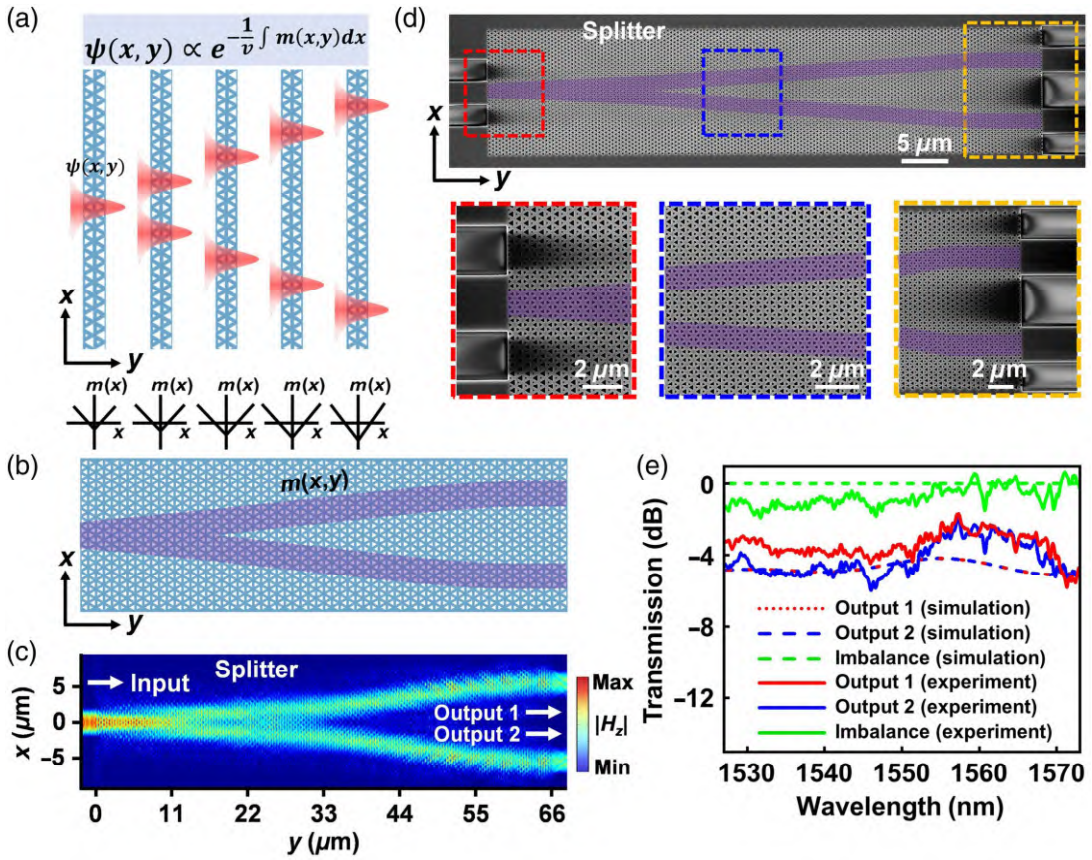

Fig. 3 Demonstration of a 50:50 power splitter based on a PMF. (a) Schematic illustration of the operation principle of the power splitter. (b) Schematic of the PhC structure of the splitter. The propagation paths of light are shaded in purple. (c) Simulated propagation profile for the PMF-based power splitter at a central wavelength of 1550 nm. (d) SEM images of the fabricated device. The purple-shaded areas indicate the propagation paths of light. The areas encircled by the red, blue, and orange dashed boxes are zoomed in and displayed at the bottom of the figure. (e) Simulated and measured transmission spectra of the power splitter.

propose and experimentally demonstrate a 2×2 directional coupler using PMFs in silicon PhCs at telecommunication wavelengths (see Sec. 13 in the Supplementary Material for details).

As the inter-valley coupling is negligible among the counter-propagating waves affiliated with different valleys, the transport of the propagative bulk states under the synthetic PMFs is topologically protected.[41,44] Here, we fabricated and measured different kinds of PhC devices (including the straight waveguide, S-bend, and power splitter) with intentionally introduced defects. The experimental details are provided in Sec. 14 in the Supplementary Material. No severe discrepancies were observed between the transmission spectra of the fabricated devices with and without defects. The experimental results show clear evidence that the performance of the PMF-based devices exhibits good robustness against small perturbations, which is very much desired in large-scale photonic integration and massive production. We also investigate the robustness of the PMF-based devices against large areas of defects. The simulation results are provided in Sec. 14 in the Supplementary Material.

2.3 High-Speed Data Transmission Experiment

To verify the feasibility of using the aforementioned devices in realistic on-chip optical communication systems, we performed a high-speed data transmission experiment[62] based on the proposed S-bend and power splitter, as shown in Fig. 4. The experimental setup and the digital signal processing (DSP) flow charts for the transceiver are illustrated in Figs. 4(a) and 4(b), respectively (for details, see Sec. 15 in the Supplementary Material). A Nyquist-shaped 70-GBaud PAM-4 signal is transmitted through each channel of the fabricated devices. The measured optical spectra of the signals before and after passing the devices are shown in Figs. 4(c) and 4(d). Figure 4(e) plots the bit error rates (BERs) for the channels of the S-bend and the splitter, which are all below the 7% hard-decision-forward error correction threshold of 3.8×10^{-3}. The recovered eye diagrams of the PAM-4 signals for different channels are presented in Fig. 4(f). The demonstration provides unequivocal evidence that the basic functional devices built with PMFs in the telecom band can be used in real applications such as on-chip optical communications.

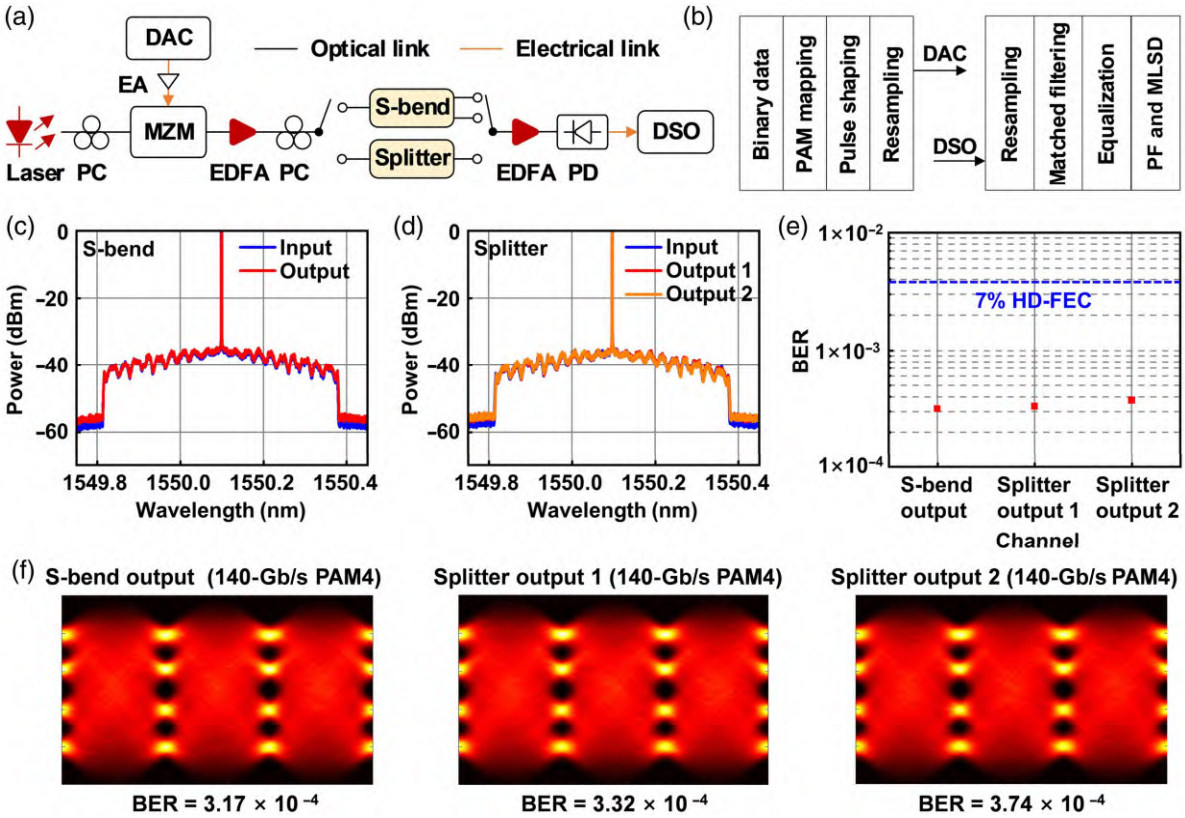

Fig. 4 High-speed data transmission experiment based on the S-bend and the power splitter. (a) Experimental setup for the data transmission of 140-Gb/s PAM-4 signals. The black and yellow lines represent optical and electrical links, respectively. PC, polarization controller; DAC, digital-to-analog converter; EA, electrical amplifier; MZM, Mach–Zehnder modulator; EDFA, erbium-doped fiber amplifier; PD, photodiode; DSO, digital storage oscilloscope. (b) DSP flow charts for the transceiver. (c) and (d) Measured optical spectra of the PAM-4 signals before and after passing the (c) S-bend and (d) power splitter. BERs (e) and recovered eye diagrams (f) of the PAM-4 signals for different channels of the S-bend and the splitter.

3 Conclusion

We have proposed a universal and systematic methodology for designing and implementing PMFs to arbitrarily control the flow of light in silicon PhCs at telecommunication wavelengths. Different from the previous works that focus on the robust transport of the Landau level states (similar to the topological edge states in topological PhCs), we investigated the evolution of the propagative bulk states under nonuniform PMFs and realized diverse optical functions such as the bending and splitting of light on a chip with high flexibility. An S-bend with a low IL (<1.83 dB) and a 50:50 power splitter with a low EL (<2.11 dB) and imbalance (less than ±0.5 dB) were experimentally demonstrated. A high-speed data transmission experiment with 140-Gb/s PAM-4 signals was also carried out to verify the applicability of these devices in practical optical communication systems. In contrast to conventional silicon waveguide devices, our PMF-based approaches show inherent defect resilience through topologically protected transport and unprecedented flexibility in device design via field-programmable light paths. Our work provides a new and highly flexible paradigm for controlling neutral particles with synthetic magnetic fields and designing nanophotonic devices with artificial gauge fields. The development of a number of PMF-based devices could be envisaged, such as power splitters with uneven splitting ratios, Mach–Zehnder interferometers, microloop resonators utilizing the spin- and valley-dependent transportation, and even wavelength multiplexing devices by introducing pseudoelectric fields simultaneously. Combining with the technique that realizes active waveguides using liquid crystals,[63] the tunable PMF-based devices can be designed for wide applications in programmable integrated optics and wearable photonics. As compared with conventional topological edge states, the Landau level states are more beneficial for device design. They do not require the breaking of time-reversal symmetry and therefore are CMOS-compatible. The propagation paths of the Landau level states can be freely customized while the propagation directions of the edge states in valley PhCs are restricted by the lattice symmetries (e.g., K and K' directions for C_{6v} symmetry). Furthermore, the symmetry-breaking perturbations such as fabrication errors can cause edge state hybridization and backscattering in valley PhCs.[64–66] In contrast, the Landau level states are less sensitive to symmetry breaking because they are induced by continuously varying the PhC structures. It could serve as a design principle for a new family of nanophotonic devices that would help us understand the behaviors of photons under

various PMFs and advance fields ranging from optical communications to optical computing and quantum information processing.

Disclosures

The authors declare no conflicts of interest.

Code and Data Availability

The data underlying the results presented in this paper can be obtained from the authors upon reasonable request.

Acknowledgments

The work was supported in part by the National Key Research and Development Program of China [Grant No. 2023YFB2905503 (L. S.)] and the National Natural Science Foundation of China [Grant Nos. 62035016 (J. D.), 62475146 (L. S.), 62105200 (L. S.), and 62341508 (Y. S.)]. The authors thank the Center for Advanced Electronic Materials and Devices of Shanghai Jiao Tong University for the support in device fabrication.

References

1. L. Landau, "Diamagnetismus der metalle," *Z. Rhys.* **64**, 629–637 (1930).
2. K. V. Klitzing, G. Dorda, and M. Pepper, "New method for high-accuracy determination of the fine-structure constant based on quantized Hall resistance," *Phys. Rev. Lett.* **45**(6), 494–497 (1980).
3. D. J. Thouless et al., "Quantized Hall conductance in a two-dimensional periodic potential," *Phys. Rev. Lett.* **49**(6), 405–408 (1982).
4. S.-C. Zhang and J. Hu, "A four-dimensional generalization of the quantum Hall effect," *Science* **294**(5543), 823–828 (2001).
5. B. A. Bernevig et al., "Eight-dimensional quantum Hall effect and "octonions"," *Phys. Rev. Lett.* **91**(23), 236803 (2003).
6. B. A. Bernevig and S.-C. Zhang, "Quantum spin Hall effect," *Phys. Rev. Lett.* **96**(10), 106802 (2006).
7. Y. Li, S.-C. Zhang, and C. Wu, "Topological insulators with SU(2) Landau levels," *Phys. Rev. Lett.* **111**(18), 186803 (2013).
8. X. Qian et al., "Quantum spin Hall effect in two-dimensional transition metal dichalcogenides," *Science* **346**(6215), 1344–1347 (2014).
9. G. Jotzu et al., "Experimental realization of the topological Haldane model with ultracold fermions," *Nature* **515**(7526), 237–240 (2014).
10. M. K. Ma et al., "Robust quantum Hall ferromagnetism near a gate-tuned $v = 1$ Landau level crossing," *Phys. Rev. Lett.* **129**(19), 196801 (2022).
11. S. Das, S. Das, and S. S. Mandal, "Fractional quantum Hall states of the phase in the second Landau level," *Phys. Rev. Lett.* **132**(10), 106501 (2024).
12. J. Wang et al., "Exact Landau level description of geometry and interaction in a flatband," *Phys. Rev. Lett.* **127**(24), 246403 (2021).
13. X.-G. Wen, "Colloquium: zoo of quantum-topological phases of matter," *Rev. Mod. Phys.* **89**(4), 041004 (2017).
14. T. Senthil, "Symmetry-protected topological phases of quantum matter," *Annu. Rev. Condens. Matter Phys.* **6**(1), 299–324 (2015).
15. T. Ozawa et al., "Topological photonics," *Rev. Mod. Phys.* **91**(1), 015006 (2019).
16. G.-J. Tang et al., "Topological photonic crystals: physics, designs, and applications," *Laser Photonics Rev.* **16**(4), 2100300 (2022).
17. Z. Wang et al., "Observation of unidirectional backscattering-immune topological electromagnetic states," *Nature* **461**(7265), 772–775 (2009).
18. Y. Poo et al., "Experimental realization of self-guiding unidirectional electromagnetic edge states," *Phys. Rev. Lett.* **106**(9), 093903 (2011).
19. F. Guinea, M. I. Katsnelson, and A. K. Geim, "Energy gaps and a zero-field quantum Hall effect in graphene by strain engineering," *Nat. Phys.* **6**(1), 30–33 (2010).
20. A. H. C. Neto et al., "The electronic properties of graphene," *Rev. Mod. Phys.* **81**(1), 109–162 (2009).
21. N. Levy et al., "Strain-induced pseudo-magnetic fields greater than 300 Tesla in graphene nanobubbles," *Science* **329**(5991), 544–547 (2010).
22. T. Low and F. Guinea, "Strain-induced pseudomagnetic field for novel graphene electronics," *Nano Lett.* **10**(9), 3551–3554 (2010).
23. C.-C. Hsu et al., "Nanoscale strain engineering of giant pseudo-magnetic fields, valley polarization, and topological channels in graphene," *Sci. Adv.* **6**(19), eaat9488 (2020).
24. P. Li et al., "Acoustic Landau levels in a synthetic magnetic field with a symmetric gauge," *Phys. Rev. A* **22**(1), 014047 (2024).
25. X. Wen et al., "Acoustic Landau quantization and quantum-Hall-like edge states," *Nat. Phys.* **15**(4), 352–356 (2019).
26. O. Jamadi et al., "Direct observation of photonic Landau levels and helical edge states in strained honeycomb lattices," *Light Sci. Appl.* **9**(1), 144 (2020).
27. M.-C. Jin et al., "Flat Landau levels and interface states in two-dimensional photonic crystals with a nodal ring," *Phys. Rev. B* **109**(5), 054108 (2024).
28. J. Guglielmon, M. C. Rechtsman, and M. I. Weinstein, "Landau levels in strained two-dimensional photonic crystals," *Phys. Rev. A* **103**(1), 013505 (2021).
29. B. Yang et al., "Nonuniform pseudo-magnetic fields in photonic crystals," *Adv. Photonics Nexus* **3**(2), 026011 (2024).
30. H. Jia et al., "Observation of chiral zero mode in inhomogeneous three-dimensional Weyl metamaterials," *Science* **363**(6423), 148–151 (2019).
31. Z. Cui et al., "On-chip elastic wave manipulations based on synthetic dimension," *Phys. Rev. Lett.* **133**(25), 256602 (2024).
32. M. Yan et al., "Pseudomagnetic fields enabled manipulation of on-chip elastic waves," *Phys. Rev. Lett.* **127**(13), 136401 (2022).
33. H. Abbaszadeh et al., "Sonic Landau levels and synthetic gauge fields in mechanical metamaterials," *Phys. Rev. Lett.* **119**(19), 195502 (2017).
34. Z. Cheng et al., "Three-dimensional flat Landau levels in an inhomogeneous acoustic crystal," *Nat. Commun.* **15**(1), 2174 (2024).
35. S. Li, P. G. Kevrekidis, and J. Yang, "Emergence of elastic chiral Landau levels and snake states," *Phys. Rev. B* **109**(18), 184109 (2024).
36. Z. Yang et al., "Strain-induced gauge field and Landau levels in acoustic structures," *Phys. Rev. Lett.* **118**(19), 194301 (2017).
37. M. C. Rechtsman et al., "Strain-induced pseudomagnetic field and photonic Landau levels in dielectric structures," *Nat. Photonics* **7**(2), 153–158 (2013).
38. H. Schomerus and N. Y. Halpern, "Parity anomaly and Landau-level lasing in strained photonic honeycomb lattices," *Phys. Rev. Lett.* **110**(1), 013903 (2013).
39. M. Bellec et al., "Observation of supersymmetric pseudo-Landau levels in strained microwave graphene," *Light Sci. Appl.* **9**(1), 146 (2020).
40. C. R. Mann, S. A. R. Horsley, and E. Mariani, "Tunable pseudo-magnetic fields for polaritons in strained metasurfaces," *Nat. Photonics* **14**(11), 669–674 (2020).
41. W. Zhao et al., "Landau rainbow induced by artificial gauge fields," *Phys. Rev. Lett.* **133**(23), 233801 (2024).
42. M. Barsukova et al., "Direct observation of Landau levels in silicon photonic crystals," *Nat. Photonics* **18**(6), 580–585 (2024).

43. R. Barczyk, L. Kuipers, and E. Verhagen, "Observation of Landau levels and chiral edge states in photonic crystals through pseudomagnetic fields induced by synthetic strain," *Nat. Photonics* **18**(6), 574–579 (2024).
44. H. Jia et al., "Experimental realization of chiral Landau levels in two-dimensional Dirac cone systems with inhomogeneous effective mass," *Light Sci. Appl.* **12**(1), 165 (2023).
45. A. Vakulenko et al., "Adiabatic topological photonic interfaces," *Nat. Commun.* **14**(1), 4629 (2023).
46. S. Kiriushechkina et al., "Spin-dependent properties of optical modes guided by adiabatic trapping potentials in photonic Dirac metasurfaces," *Nat. Nanotechnol.* **18**(8), 875–881 (2023).
47. K. Chen et al., "Photonic Dirac cavities with spatially varying mass term," *Sci. Adv.* **9**(12), eabq4243 (2023).
48. Y. Yang et al., "Photonic Dirac waveguide in inhomogeneous spoof surface plasmonic metasurfaces," *Nanophotonics* **13**(20), 3847–3854 (2024).
49. M. I. Shalaev et al., "Robust topologically protected transport in photonic crystals at telecommunication wavelengths," *Nat. Nanotechnol.* **14**(1), 31–34 (2019).
50. H. Wang et al., "Ultracompact topological photonic switch based on valley-vortex-enhanced high-efficiency phase shift," *Light Sci. Appl.* **11**(1), 292 (2022).
51. S. Barik et al., "Two-dimensionally confined topological edge states in photonic crystals," *New J. Phys.* **18**(11), 113013 (2016).
52. H. Wang et al., "Asymmetric topological valley edge states on silicon-on-insulator platform," *Laser Photonics Rev.* **16**(6), 2100631 (2022).
53. L. Sun et al., "Thermally tunable add-drop filter based on valley photonic crystals for optical communications," *Nanophotonics* **13**(24), 4459–4470 (2024).
54. X.-T. He et al., "A silicon-on-insulator slab for topological valley transport," *Nat. Commun.* **10**(1), 872 (2019).
55. T. Ma and G. Shvets, "All-Si valley-Hall photonic topological insulator," *New J. Phys.* **18**(2), 025012 (2016).
56. X.-D. Chen et al., "Valley-contrasting physics in all-dielectric photonic crystals: orbital angular momentum and topological propagation," *Phys. Rev. B* **96**(2), 020202 (2017).
57. A. Messiah, *Quantum Mechanics*, Courier Corporation (2014).
58. Y. He et al., "On-chip metamaterial-enabled high-order mode-division multiplexing," *Adv. Photonics* **5**(5), 056008 (2023).
59. L. Sun et al., "Broadband and fabrication tolerant power coupling and mode-order conversion using Thouless pumping mechanism," *Laser Photonics Rev.* **16**(11), 2200354 (2022).
60. Y. Su et al., "Silicon photonic platform for passive waveguide devices: materials, fabrication, and applications," *Adv. Mater. Technol.* **5**(8), 1901153 (2020).
61. C. Lu et al., "On-chip nanophotonic topological rainbow," *Nat. Commun.* **13**(1), 2586 (2022).
62. J. Li et al., "Silicon photonic carrier-assisted differential detection receiver with high electrical spectral efficiency for short-reach interconnects," *J. Lightwave Technol.* **41**(3), 915–925 (2022).
63. T. Wei et al., "Liquid-crystal-mediated active waveguides toward programmable integrated optics," *Adv. Opt. Mater.* **8**(10), 1902033 (2020).
64. D. Yu, S. Arora, and L. Kuipers, "Impact of transforming interface geometry on edge states in valley photonic crystals," *Phys. Rev. Lett.* **132**(11), 116901 (2024).
65. H. Xue, Y. Yang, and B. Zhang, "Topological valley photonics: physics and device applications," *Adv. Photonics Res.* **2**(8), 2100013 (2021).
66. M. B. de Paz et al., "Engineering fragile topology in photonic crystals: topological quantum chemistry of light," *Phys. Rev. Res.* **1**(3), 032005 (2019).

Pan Hu is a PhD student at the State Key Laboratory of Photonics and Communications, Shanghai Jiao Tong University. His research interests include topological photonics, silicon photonics and nanophotonics.

Lu Sun received his BS and PhD degrees from the Shanghai Jiao Tong University, Shanghai, China, in 2011 and 2016. He was a postdoctoral fellow at the University of Toronto, Canada. He is now an associate professor at Shanghai Jiao Tong University. His research interests include topological photonics, silicon photonics and nanophotonics. He has published more than 50 journal and conference papers.

Biographies of the other authors are not available.